SIMULATION OF ACTIVE TWIST ROTOR BLADES USING A THERMAL ANALOGY METHOD IN HMB3

R. Steininger, r.steininger.1@research.gla.ac.uk, University of Glasgow, United Kingdom
G. N. Barakos, george.barakos@glasgow.ac.uk, University of Glasgow, United Kingdom
M. A. Woodgate, mark.woodgate@glasgow.ac.uk, University of Glasgow, United Kingdom

Abstract

Helicopters vibration is a well-documented area with the main rotor identified as a key source. A proposed mitigation is based on active rotor blade twist. This promises a reduction in noise and vibration, specially via avoidance of BVI effects, and has some potential for power reduction. For the development and certification of such devices, there is a need to accurately simulate the twist actuators, and rotor structure within a high-fidelity CFD framework. Two structural modelling approaches for rotors in forward flight are compared in this work. A conventional, one-dimensional, beam model is typical, where the static and dynamic twist is applied via rigid rotations on the blade. The second approach uses a medium-fidelity structural model made of 3D elements, where the active twist piezoelectric actuators are modelled via a thermal analogy method. This work presents a comparison of the two approaches.

1 Introduction

In recent years, active rotors with on-blade mechanisms have been investigated to reduce vibrations and improve rotor efficiency. One proposed solution is active blade twist.

The capability for required high-frequency twist strain has been demonstrated using embedded piezoelectric actuators in experimental [1–4] and full-scale rotors [5]. Active elements promise a reduction in noise and vibration, specially avoidance of BVI effects, and potential for power reduction. An active twist allows to change the blade twist to best suit the flight condition and use harmonic actuation to affect the local angle of attack and the tip-vortex miss distance. For the development and certification of such devices, there is a need to accurately simulate the twist actuators and the rotor structure within the CFD framework, one such method is presented here.

Blade structural design is a significant challenge, with aerodynamicists targeting thinner and higher aspect ratio rotor blades in some applications. Achieving the required bending and torsional rigidity within a given outer mold line, competes with the goal of decreasing the blade weight. Due to the centrifugal stresses, additional blade mass requires a large amount of additional blade strength. Blade structural designs are validated either by FEM models or by sectional analysis. An example of a sectional analysis tool is VABS by Analyswift, where recently efforts have been made by Purdue University and US Army to use artificial intelligence to optimise the internals of the blades [6]. It operates through loops of structural design and analysis, similar to how a human designer would act.

Presented at 49th European Rotorcraft Forum, Germany, 5-7th September, 2023.

Loose, iterative coupling of rotor structural analysis and fluid dynamics simulations are widespread in the rotorcraft field. The rotor blade structural response, often paired with a kinematic body model, is computed from airloads until a periodic, trimmed state is found. The displacements are then transferred back to the CFD, until the unsteady solution reaches a periodic state, with the two steps repeated until two updates are within a desired margin. In this work, two structural modelling approaches for rotors in forward flight are compared for an active twist rotor. The first method is a one-dimensional, non-linear beam model, where the static and dynamic twist is applied via rigid rotations on the reference blade before the structural deformation of the mesh. The second method uses a medium-fidelity structural model made of 3D elements, where the active twist piezoelectric actuators are modelled via a thermal analogy method. The models are compared using loads extracted from the inhouse CFD solver HMB3 (Helicopter Multi Block 3). The generation of the aerodynamic loads is presented in Section 4.

2 Structural Analysis in NASTRAN

The structural analysis techniques employed in rotor analysis vary due to requirements of accuracy, analysis speed and available data. Often, simplified 1-dimensional beams, where properties of structure and mass are applied at set stations, are employed in rotorcraft simulations. These models can integrate a hub-approximation including the hinges and the pitch links. They are often natively integrated with low- and mid-fidelity aerodynamic tools, but can also be coupled to CFD. However, there are limitations to the accuracy of beam structural models. At the cost of computational expense and meshing time, the root and aerofoil portions of the rotor blade can be analysed using the 3-D Finite Element Method (FEM). This method allows to directly model on-blade actuators and can take spanwise variatons better into account. FEM also allows the extraction of blade stresses and can model corner stresses where cut-outs exist.

With many structural solvers such as NASTRAN, a large number of parameters and different analyses can be set. In static deflection problems, linear and non-linear analyses are available. Reduced shear models are available, which avoid overly stiff thin elements, while not introducing zero-energy modes in the solution. Shear bubble functions can be selected to reduce this effect for large displacements, but come at an increased computational cost. These methods are further described in the NASTRAN reference manuals. To validate rotor blade models and compare with test data or other models, the structural Eigenmodes can be extracted from modal analyses. The modes and frequencies can be used to calculate the blade motions in hover and forward flight in weak- or strongly coupled algorithms, with some limitations. Besides this, transient response modelling with tables of aerodynamic loads and actuator positions can be used for CFD-CSD simulation. This type of analysis has a weak coupling to CFD and requires sequential iterations, but allows for higher structural fidelity and direct actuator modelling.

2.1 Linear Static Analysis

For small forces and deformations, at long timescales, a linear static simulation may be appropriate. The preconditions for this are linear force-deformation and stress strain responses of the structure, and ignores effects of inertia. All stresses must be below the yield stress. In NASTRAN, this solution type is performed with SOL 101, but can also be done using SOL 400 by specifying a *STATICS* type of analysis. The stiffness matrix $\mathbf{K}$ stays constant through the whole analysis, so no iterations are done. This includes the boundary conditions and the forces of the problen. The relationship between the force vector $\mathbf{P}$, the stiffness matrix and the displacement vector $\mathbf{u}$ is linear:

$$\mathbf{P} = \mathbf{K}\mathbf{u} \tag{1}$$

The displacement vector is obtained by inverting the stiffness matrix. The principle of superposition applies to loads and displacements.

2.2 Non-linear Static Analysis

When the physical problem contains large structural deflections, non-linear materials or possible contacts between parts, linear analysis is not suitable. In non-linear problems, the stiffness matrix $\mathbf{K}$ depends on the loading and displacement vectors in addition to the structural properties, geometry and boundary conditions.

$$\mathbf{P} = \mathbf{K}(\mathbf{P}, \mathbf{u})\mathbf{u} \tag{2}$$

The final displacements cannot be solved for directly, and iterative schemes are required, where the non-linear material properties are updated, based on the element deformations of the last iteration. Every iteration step also requires for the stiffness matrix to be inverted, adding to the computational time.

Non-linear static analysis in NASTRAN is executed with SOL 106 or 400, specified via *NLSTATICS* keyword.

2.3 Modal Analysis

Eigenmode extraction for modal analysis methods requires a non-linear analysis to build the stiffness matrix, before frequencies and shapes can be extracted. The stiffness matrix is assumed to be symmetric and therefore orthogonal Eigenvalues can be extracted, which contain the frequencies and shape vectors. The usage of these modes in CFD-CSD coupling is explained in Section 4.1. NASTRAN supports the calculation of the modes in *SOL 103, 106* and *400*. Method 103 calculates the modes directly from the stiffness matrix, which makes it unsuitable for pre-stressed components, such as the rotor under centrifugal load. The centrifugal stiffening can be added through a subcase of linear-static analysis. SOL 106 natively accounts for the loading on the mode output when a previous non-linear statics result is taken as the initial solution of the modal type analysis. Similarly, SOL 400 analysis allows for a linear, or non-linear static analysis or any other types of analyses to be chained with the modal analysis, making it also suitable. The implicit SOL 400 method supports parts with contact boundary conditions, which 106 does not.

2.3.1 Sources of Non-linearity

A common source of non-linearity in structural analysis arises from the material properties. Within the time-frame of the analysis, most materials follow a linear, spring-like relation between stress and strain below the yield stress. The stiffness is the Young's modulus. Going beyond this stress, materials undergo plastic deformation, where the molecular and/or crystal structures start to rearrange. The stress-strain relationship turns non-linear, often increasing strain disproportionately to the stress, until failure. Over long time-spans under load, materials such as plastics undergo creep, where the strain is dependant on time and stress, and may undergo hysteresis. Other material non-linearities can come from kinematic hardening or viscoplasticity. Such non-linearities are not considered here.

Geometric non-linearities are problems of large displacements. The flap bending angles experienced on rotor blades, may require a non-linear analysis. Linear analysis methods based on small angle approximations might not sufficiently capture the non-linear relation between strain and displacements. Other geometric non-linearities like buckling or snap-through are rare in rotorcraft applications, as these conditions are generally avoided. However, some on-blade actuators may exploit snap-through characteristics to avoid constant power draw during deployment.

Non-linearity can also arise from boundary conditions. Forces may change in amplitude, direction and application area, depending on structural deformations. As a rotor flaps and bends, the centrifugal force angle changes with respect to the finite elements. Iterative methods are required to resolve and update the force equilibirum. Other boundary condition non-linearities can arise from parts coming in contact or friction.

2.4 Structural Elements

In MSC NASTRAN, structral elements are denoted with a "C" prefix, while properties of such elements are entered by commands with the "P" prefix. Examples are CBEAM, CTETRA, PBEAM, PSOLID, PCOMP. Types of beam elements can be mixed in the structural analysis, within reason. Where rigid connections need to be made, such as a between the hinge point and the surface layer of the blade root, rigid bar elements or similar (RBAR, RBE) can be employed.

2.4.1 Beam-Element CBEAM

The beam element (CBEAM) includes the properties of area, moment of inertia in flap and lag, torsional stiffness, mass/length and the locations of the centre of gravity and elastic axis and pre-twist angle at both ends of the beam and at any intermediate stations. Concentrated and distributed loads can be applied to the beam. Non-linear material properties can be applied if necessary. The beam elements are defined as a line between two grid points, and the axial rotation is defined via two planes collinear with the axis. Their axes are explained in Figure 1. The beam forms the elastic axis (shear centre), and the offsets for the neutral axis (tension centre) and mass axis (centre of gravity) can be provided at any beam location. However, since the structural properties are given with respect to the direction of the beam, large differences between the elastic axis' angle and the beam cross-section will introduce errors. Three-point beams are also available, where a middle point is specified for a beam with quadratic curvature.

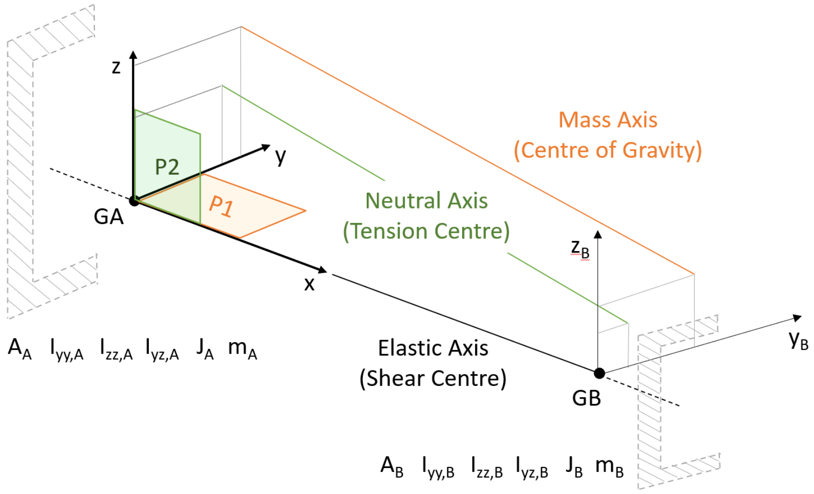

Figure 1: NASTRAN two-point CBEAM axes and properties.

2.4.2 Volume-Elements CTETRA, CPYRAM, CPENTA, CHEXA

The 3D finite element model is made from volume elements. The elements can be defined with linear edges, two points per edge, or as second order elements made from three points per edge. The structural and non-structural mass properties are automatically calculated from the element shape, size and assigned material density. The material properties can be provided as anisotropic or isotropic, including thermal properties. For parts made of composite materials, orthotropic properties can be provided in the preferred local or global reference frame. With the properties of a single composite layer, the overall material properties can be automatically calculated when the layup order and directions are provided. Example hexa and penta elements are shown in Figure 2, where the Gaussian collocation points are marked orange.

Two integration schemes were considered in this study, and compared in Section 5.1. The integration scheme can be changed on a part-per-part basis. The first model is a 2×2×2 standard isoparametric integration scheme. The load and deformation distributions follow the same order as the element edges. Under-integration can be used to solve the problem quicker, however at a loss of accuracy due to introduction of zero-energy modes. The 2×2×2 under-integration scheme with reduced shear and is availble for high aspect-ratio cells to avoid hourglassing and shear locking and is also compared. The FEM model was constructed to inherently avoid cells with these problems. Over-integration is also available, where the elements may better resolve steep gradients such as in corner stresses at the expense of increased cost. This method, however, can result in elements with unrealistically high stiffness.

3 Structural Model Creation

A 1D-beam model and an approximate 3D finite element model were created in this study. Beam models usually involve modelling of the blade hub assembly using rotational spring/damper elements, and rigid, or elastic beams along the radius. Typically, ten or more beam sections are used. Each beam element carries cross-sectional properties at the beam ends, which are interpolated along its length. The blade cross sections are simplified to their representative properties. Large cross section, full carbon fibre blade roots can be simplified to rigid elements and twist actuators can be modelled only by applying moments at beam cross-sections or by rigidly prescribed torsion. Finite Element structural models consist of volumetric or area parts, which carry the structural properties of the materials they are made of. The blade cross-section is fully modelled and may consist of several elements. Depending on the available data for the blade volume, the blade can be accurately represented along the full span without any interpolation. Pressure tapping locations and other details of the structure are carefully contained. Active twist can be modelled as on the beams, or alternatively by modelling the actuators. The actuators produce a strain due to the input-voltage. The piezoelecetric relation can be simulated by manipulating the thermal-expansion coefficients of the actuator material and prescribing component temperatures. This is called the Thermal Analogy Method (TAM) and is described in Section 3.3. NASTRAN SOL 106 and SOL 400 non-linear analysis methods were used to evaluate the structural response. Cen-

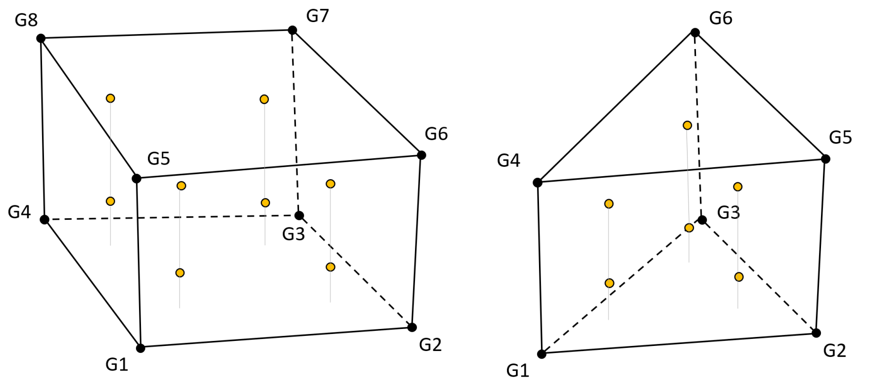

(a) CHEXA(8) element (a) CPENTA(6) element

Figure 2: NASTRAN CHEXA(8) and CPENTA(6) elements with the standard Gauss collocation points.

trifugal stiffening was also introduced.

3.1 1-D Beam

A beam model was created in MSC NASTRAN to analyse the structural dynamics of the STAR (Smart Twisting Active Rotor) [3] blade assembly to be used with the HMB3 CFD solver. The NASTRAN elements of the 1D-beam model are shown in Figure 3. 108 beam elements were used, due to their low computational cost and to simplify deformation extraction to the fluid dynamics solver. The flap-lag hinges at the radial position of 3.75% R were approximated with a lag-spring of $3000\,\mathrm{Nm/rad}$ and a lag-damper of coefficient $\zeta = 0.5$. The pitch link was assumed rigid. The values have been chosen in accordance with the initial estimations of the experimental rotor hub. The rotor was considered rigid inboard of the lag-flap hinge. The grid points for the beam elements were all defined on the quarter chord location, which is a straight line from the centre of rotation. For each point, two additional points have been defined ahead of the leading edge and behind the trailing edge. Between these outer points, rigid bar elements were inserted. These elements had no mass or other structural properties and are only used to visualise deformations and to to interpolate the resultant forces from the CFD grid onto the structure. CBAR beam elements represented the rotor blade. An additional flap spring with small stiffness (10 Nm/rad) was required for the rigid flapping mode to converge to a steady solution. The input (.bdf) file contained the solving algorithm (SOL) and includes the bulk data entry for the blade elements and parameters.

The sectional properties were provided by DLR to the project partners and obtained from a structural simulation [7]. A preview of these properties is shown in Figure 4. The figure also shows how the sectional properties were interpolated onto the beam elements. The properties are almost constant over the length of the span beside the blade root. Small reductions in the blade stiffness can be seen at the radial stations of pressure sensors, and larger reductions where a large number of pressure sensors reduce the spar cross-section. The centre of gravity is mostly constant over the span, but changed drastically where added features like sensors may be placed.

3.2 3-D Finite Element Method

The 3D-FEM model created in this work approximates the shape of the STAR experimental rotor, based on [7] with several assumptions made, as will be discussed. The rotor blade has 15 upper and 15 lower side actuator patches, spanning the majority of the chord [7]. The actuators build the outermost layer of the aerofoil shape, and the continuous blade skin is placed underneath these. This is illustrated in Figure 5. The spanwise gaps between the actuators are filled with a second layer of the skin material, and contain cut-outs for pressure sensors [7]. The rotor blade also features trailing edge spar strips.

The leading edge spar runs along the full rotor blade and starts at the mounting region of the root. It tapers until it reaches its final shape at 22% R, from where it is constant until the tip endplate is reached. The finite element mesh was extruded from an approximate 2-dimensional cross section shown in Figure 6 (a) and is a rough approximation of the real blade used here for comparison with the beam model. The resulting prism elements keep the degrees of freedom as low as possible, while maintaining good cell quality. Initially, just the spar and nose-weight were modelled for a mesh refinement study, shown in Section 5.1.

The 2D-sections of the different components were separately meshed with similar sizing, and then

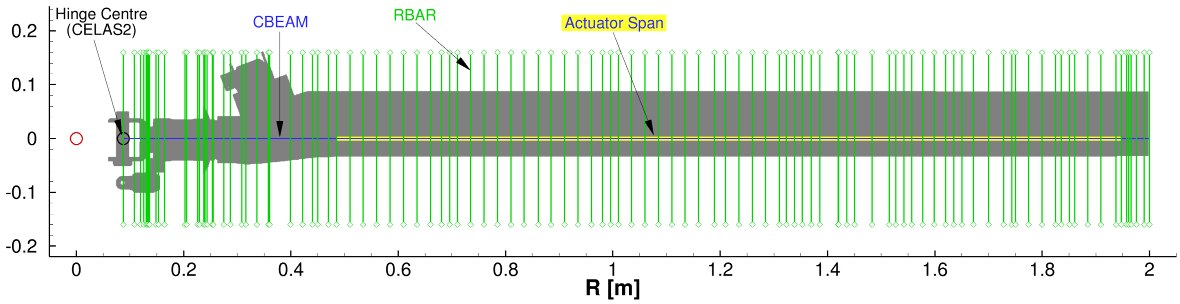

Figure 3: STAR rotor blade beam model structure. The rotational centre is at (0,0).

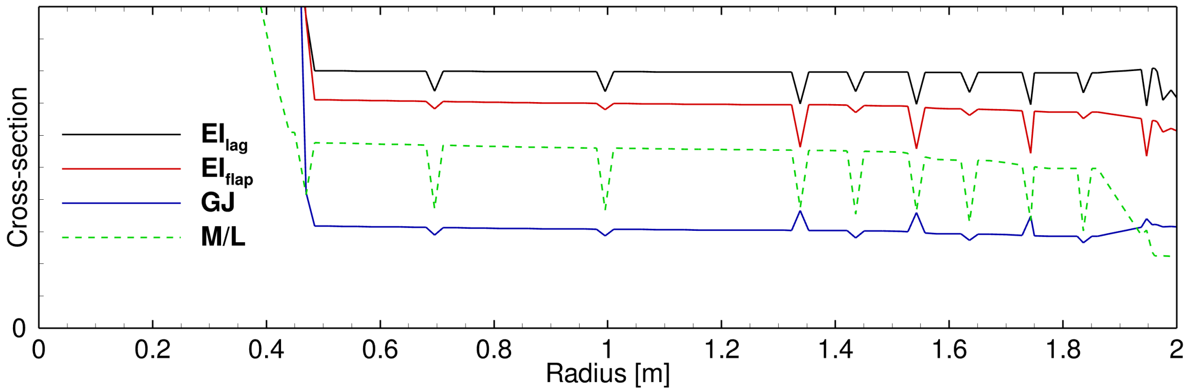

Figure 4: STAR rotor spanwise structural properties with all axes starting at zero.

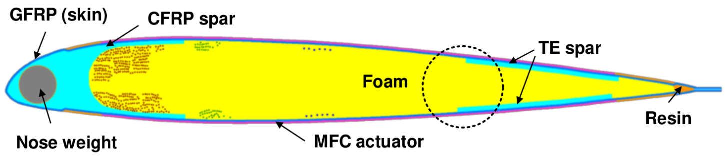

Figure 5: STAR rotor blade cross section diagram near 65% span, from tomography [7].

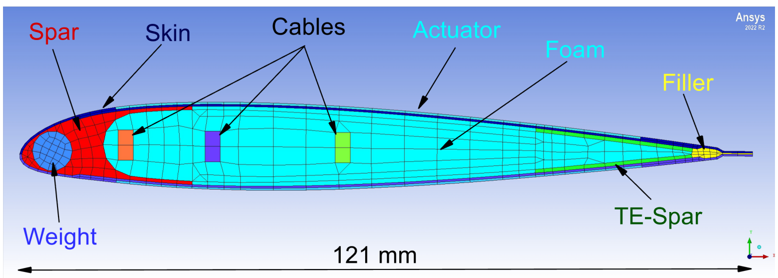

(a) Mesh section.

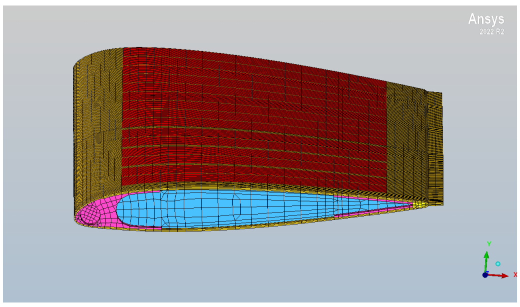

(b) 3D-model.

Figure 6: Approximate rotor 2D-section based on [7] and extruded 3D-FE model.

merged into a continuous meshed surface. The different materials were flagged in the cross-section, and spanwise variations were introduced similarly by changing the mesh part ID. This way, the actuators and nose weight could be discontinued at the relevant sections. Notably, the approximate cross section includes a simplification of the blade internal cables. The cable bundles, as seen in the CT-images, were simplified into three rectangular regions. The stiffness properties of the cables were not considered for simplicity. From the materials and geometry suggested in [7], the weight of these cables was estimated as 44 grams. Of the remaining cable weight, 190 grams was added to the concentrated root mass, and the remainder was split up between the forward pressure sensor cables and the strain gauge cables in the centre. The masses of the cables were evenly distributed along the full blade length, at approximate positions for their combined centres of gravity.

The extruded FEM-model, with the actuators visible, is shown in Figure reffig:fullfem (b). The material properties from [7] were used. A simplified geometry was created to estimate the weight of the stiff blade-root area, which was added as a concentrated mass. The total blade weight added up to 3.041 kg grams, which is slightly above the measured value of the CT-scanned blade (2.999 kg) in [7]. The complete FE model has 315k degrees of freedom.

3.3 Thermal Analogy Method

Modelling of the piezoceramic actuators is not natively supported in NASTRAN. However, it is possible to define material properties, which have temperature-strain relation. Piezoelectric coefficients can be reformulated from a voltage-strain relation via a thermal analogy method. Macro Fibre Composite (MFC) actuators [8] rely on the d33-effect, where the piezoceramic fibres are strained along their length. Considering only the d33-effect, the relationship between temperature and strain becomes:

$$d_{33}\frac{\Delta\psi}{t} = \alpha\Delta\Theta. \tag{3}$$

The equation uses the value of the d33-coefficient, the applied voltage is $\Delta\psi$, t is the actuator thickness, α is the thermal expansion coefficient and $\Delta\Theta$ is the temperature increase to apply in the model. The thermal analogy method can however not be used inversely as a strain gauge using this method.

4 Flow Solver

The computational fluid dynamics simulations were computed using the Helicopter Multi-Block 3 (HMB3) in-house software tool. It is a finite volume solver on structured multi-block grids [9]. An overset grid method is used. HMB3 solves the Unsteady Reynolds Averaged Navier-Stokes (URANS) equations in integral form using the Arbitrary Lagrangian Eulerian (ALE) formulation for time-dependant domains, including moving boundaries. To evaluate the convective fluxes, the Osher [10] approximate Riemann solver is used, while the viscous terms are discretised using a second order central differencing spatial discretisation. The MUSCL approach developed by Leer [11], is used to provide high-order accuracy in space with the alternative form of the Albada limiter [12] in regions of large gradients. Implicit, dual-time stepping method of Jameson [13] is employed. The linearised system of equations is solved using the Generalised Conjugate Gradient method with a BILU factorisation as a pre-conditioner [14]. One-equation to four-equation turbulence models are available in HMB3 solver. The 1994 k-ω SST model of Menter [15] is used for the computations presented in this work. The hover out of ground effect (OGE) simulations in HMB3 use the Froude boundary condition. A rotational quarter of the rotor domain is simulated with periodic boundary conditions, when using the steady formulation. The rotational velocity component in the rotor is created by a source term in the ALE (Arbitrary Langrangian Eulerian) discretised Navier-Stokes equations.

4.1 Coupling between CFD and CSD

For aeroelastic hover simulations, the time-independent beam analysis in MSC NASTRAN is coupled with HMB3. After a set number of steady hover simulation steps, the aerodynamic loads are extracted and converted to the reference frame of the beam model. A non-linear beam analysis in MSC NASTRAN, using solvers SOL 106 or SOL 400, calculates the displacement and rotation of the rotor beam or FEM-model. The structural model contains dense point cloud of the rotor CFD surface. From the deformation vectors of the point cloud, the rotor surface is deformed via an inverse distance weighting method, before the volume of the near blade grid is deformed similarly. The cell quality is preserved for the small angles experienced in most rotor cases, when using this method with adequate interpolation parameters.

For time-dependant problems, two solution methods are available in HMB3. A modal method and a transient response method. In the former, the first 9 structural modes of the beam-model, including the hinge modes, are incorporated in the forward flight simulation using a modal decomposition at every time-step:

$$\phi = \phi_0 + \sum_{i=1}^{n_m} \alpha_i \phi_i. \tag{4}$$

ϕ represents the deformed rotor shape and α_i, ϕ_i are the modal coefficients and mode shapes. The mode shape amplitudes α_i are computed by solving the mass-spring damper equivalent,

$$\frac{\partial^2 \alpha_i}{\partial t^2} + 2\zeta_i \omega_i \frac{\partial \alpha_i}{\partial t} + \omega_i^2 \alpha_i = f_i(t), \tag{5}$$

where ζ_i and ω_i are the mode damping factor and eigenfrequency and f_m is the forcing function. A damping factor of 0.7 would make the mode critically damped, but in practice this factor is reduced to 10% or less for the structural bending modes, to simulate the limited structural damping in the material. Due to the orthogonality of the modes, the forcing function at every degree of freedom is the dot-product of the pressure-force at a point $\mathbf{P}$ and the mass-scaled eigenvector $\phi_s(p)$:

$$f_i(t) = \sum_{p=1}^{n_s} \mathbf{P}(p,t) \cdot \phi_i(p), \tag{6}$$

where p are the discretised FEM points of the eigenmode. It is a strongly coupled method. The active elements on the blade can be simulated as an independant torsion mode, with a given amplitude and added via superposition. However, in this work, the active twist in the modal method is simplified to a rigid deformation of the blade grid, based on expected deformation values.

The second method iteratively exchanges airloads and deformations after full revolutions of the rotors. A periodic time-history of blade loads are created from CFD for every point on the blade. The loads are loaded into NASTRAN, where the transient response is computed with these loads, until a periodic deformations are obtained. The deformations are then applied to the fluid solver grid, where they are simulated until convergence. This method is weakly coupled and does not guarantee that the structural solver and airloads settle to a single periodic state. The on-blade actuators can be accurately modelled by including tables of temperature, which are a thermal analogy to voltage of the piezoactuators. The strains of the actuators directly deform the rotor blade, and can simulate reduced actuator effectiveness at high twist due to the increasing strain energies.

The employed high-fidelity rotor blade CFD grid is shown in Figure 7. It is a structured multiblock-grid. The boundary layer is fully resolved, resulting in a first cell height of 1×10^{-5} chords. The rotor blade mesh is overset on a background grid using a chimera method. The chimera boundary of the rotor blade mesh is spaced at 5% chord, matching the background grid in the near tip region.

5 Results and Discussion

5.1 Mesh-refinement study

The main-spar and the nose weight have been produced in three mesh-sizes, to estimate the computational performance and the impact on the result. A baseline 2-dimensional shape with good cell quality was designed and then extruded along the length of the beam. The cell sizes in the 2D sections were between 0.5 and 2.5 mm edge length. The spanwise extrusion was done with 15 (coarse), 5 (medium), and 1 mm (fine) prism lengths. Another mesh with a roughly 4x coarsened 2D section was also tested with the coarsest spanwise spacing. The sections are shown in Figure 8. The degrees of freedom (DoF) for these cases were: 117k, 355k, 1.77m and 70k, with a corresponding impact on computational time and memory requirement. The finest mesh required 15GB of memory for a non-linear static calculation of the spar, using SOL 400. A testing load was applied to the beam with streeses and displacements calculated using the SOL 400 non-linear statics configuration. The load is a spanwise-quadratically increasing body force, approximate to a hover load. Figure 9 shows the results of the comparisons. The $2 \times 2 \times 2$ isoparametric integration shows increasing deflections with a peak bending up to 170 mm at the tip with mesh refinement. This suggests, that longer elements lead to an artificial stiffening of the structure. The analysis was repeated with the $2 \times 2 \times 2$ under-integration scheme, with reduced shear and the bubble function of NASTRAN. This scheme is the NASTRAN default for polynomial volume elements. All mesh refinement steps provided the same result as the finest mesh in the isoparametric integration. The under-integration scheme required less CPU time for the same grid size. Therefore, the coarsest spanwise stepping was chosen for 3-dimensional parts, together with the under-integration scheme.

The impact on CPU wall-clock time, running as a

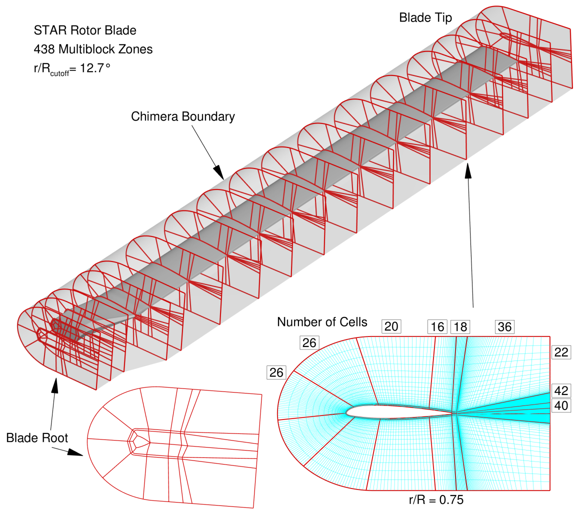

Figure 7: Near-body CFD grid.

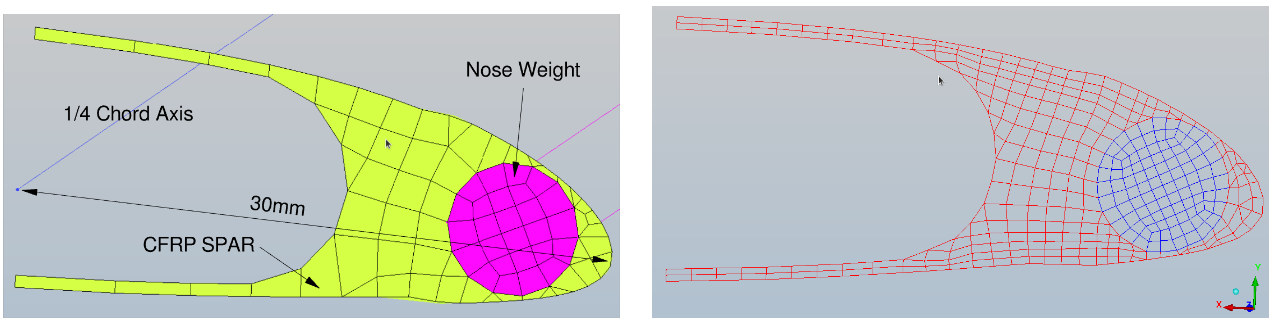

(a) Medium (70k DoF)

(b) Fine (117k-1.77m DoF)

Figure 8: FE grids (medium, fine), used for the 3D spar approximation.

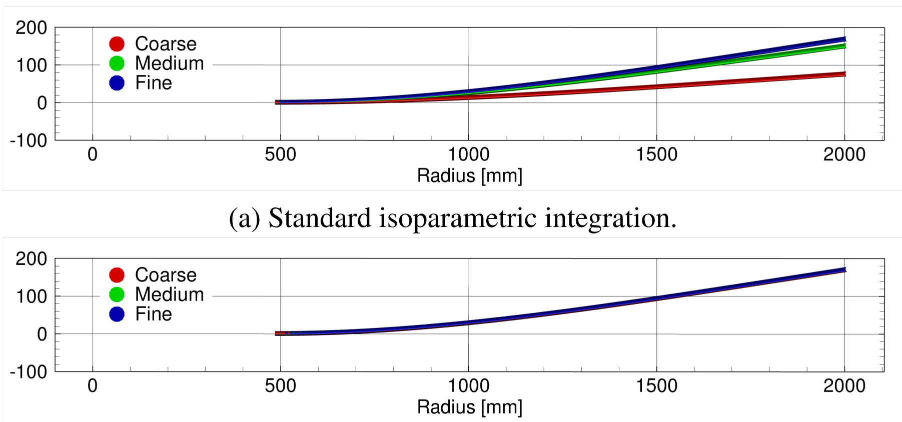

(a) Standard isoparametric integration.

(b) Under-integration with reduced shear formulation.

Figure 9: Blade structural response obtained using different mesh refinements and integration methods.

Table 1: Modal frequencies obtained using different solution strategies.

	ω/Ω_{ref} ($\Omega = 0$ Hz)		ω/Ω_{ref} ($\Omega = \Omega_{ref}$)	
SOL	106	103	106	103
F1	0.04	0.04	0.39	0.38
L1	0.27	0.27	1.01	1.01
F2	0.62	0.62	2.41	2.41
T1	1.92	1.92	3.62	3.62
F3	3.39	3.39	4.05	4.05

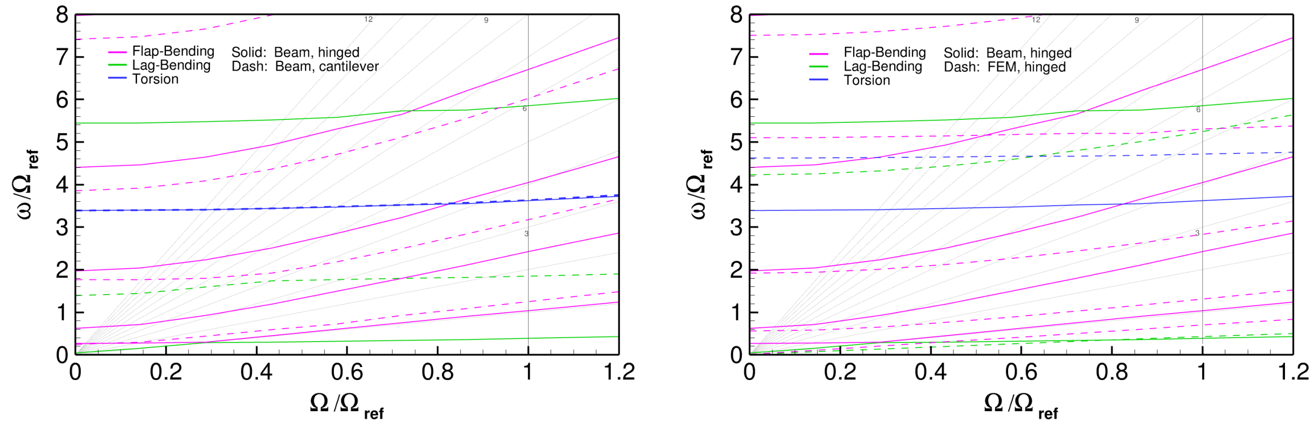

(a) Beam models

(b) Beam vs FE model

Figure 10: Comparison of modal frequencies for the beam model and the FE model. The modes are split by colour, the models by solid and dashed lines.

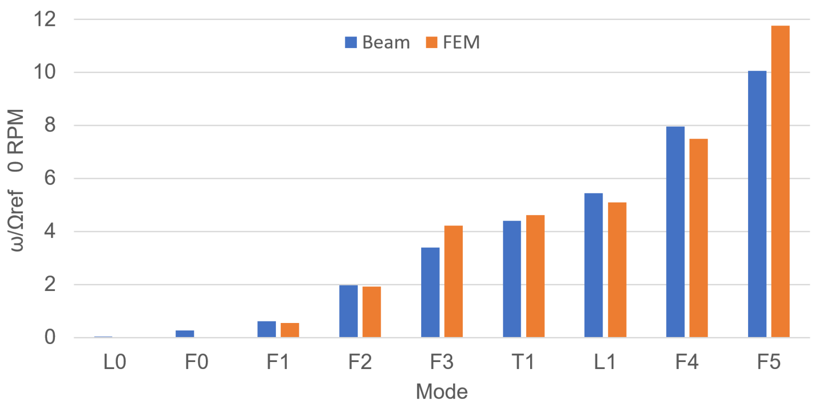

Figure 11: Eigenfrequencies of the beam model and the FEM-spar.

single-threaded process, was also evaluated. The time to complete a SOL 106 non-linear static analysis for the 117k, 355k ($3\times$), 1.77m ($15\times$) DoF models were 38s, 124s ($3.26\times$) and 824s ($21.7\times$). The models were rigidly fixed in a cantilever position and centrifugal loads were applied. To determine the effect of the simulation complexity, the 315k DoF complete blade model was also measured in SOL 106. In the cantilevered and hinged configurations, the time to resolve the non-linear static deflection was 43 seconds for the non-rotating case. When the centrifugal loads were applied, the cantilvered case was finished in 160 seconds ($3.7\times$). The rotating, hinged case took 1 hour, 10 minutes and 51 seconds to complete ($\approx 100\times$). The computational effort increases non-linearly with the degrees of freedom in the model, in part to increasing demand on the memory and storage. A strong dependance between computational effort and problem non-linearity can also be observed, as the complex cases require many additional iterations and load-step increments.

5.2 Structural Eigenmodes

The structural eigenfrequencies of the beam model in the hinged and cantilevered configurations are compared in Figure 10. Both were obtained using solution sequence 106, which executes a modal analysis on the stiffness matrix after a non-linear static solution step. They do not necessarily represent the frequencies of the experimental rotor, which was adapted since the creation of the sectional properties from FEM sectional analysis. The first flapping mode of the hinged spar case has a linear frequency increase with rotor RPM. This is because the centrifugal force contributes the majority of the forcing function. The first lag mode is mostly constant due to the hub lag damping and springs attached to the root of the blade. The third flap and first torsion mode are cross coupled and cannot fully be separated from each other. Similarly, the higher freuquency modes deviate from pure flap, lag and torsion mode with a large amount of coupling, making them difficult to categorise. The blade with the clamped root showed higher eigenfrequencies in flap-bending and chord bending. The first torsion mode was determined as unchanged from the hinge condition, where root torsion is equally constrained.

The hinged spar case was also compared to solution sequence 103, which is a pure modal solver. To obtain a result for the centrifugally stiffened case, the analysis was chained to a non-linear statics analysis in the same mode. The difference in the result is negligible, as shown for the first 5 mode frequencies of Table 1.

The approximate FEM model with hinges was also analysed using SOL 106. The comparison to the beam model is presented in Figure 10 (b), where the FEM model data uses dashed lines. The rigid lag mode is very closely aligned to the beam model, as expected. In the non-rotating condition, the first modes of the FEM model are in reasonably good agreement with the beam. The non-rotating frequencies are presented in a Figure 11. Generally, the torsion modes are around 20% stiffer in the 3D-model. At higher rotation speeds, the centrifugal stiffening is predicted to be less on the FEM blade. This result is possibly due to the uncertainties and simplifications made to the material properties, which are mostly isotropic. The order and the shapes of the modes agree between the models, and some of the modal coalescence could be observed on both models.

6 Conclusions and future work

In this work, tests of finite element modelling for MSC NASTRAN have been conducted to build best practices for a complete FEM active blade model. It was found that accurate pre-load of the stiffness matrix is required to predict the rotor modal frequencies on both beam and FEM models. A FE mesh refinement study was conducted for the main spar of the rotor blade, where the finest grid spacing of 1.77m degrees of freedom (DoF) was found the be fully resolved using the isoparametric integration scheme. However, the reduced shear under-integration, formulated to reduce hourglassing and shear locking could produce the same result on the coarsest grid of 70k DoF. Load-vector updates are crucial to produce the correct deflections in both static and eigenvalue analysis, and may only be ignored at very small angles of deflection. The rotor eigenfrequencies and shapes of the beam model analyses matched very well. The blade FEM model showed the same modal order as the beam model, however with a generally stiffer torsion mode, while other mode frequencies were lower. Closer correlation between the results was expected, and some error may be introduced by insufficient modelling of the isotropic materials. The thermal analogy method was defined, but modelling could not yet be finished on the FEM model.

In the future, further work will address:

- the uncertainties regarding material properties, fibre alignment and material isotropy,
- the correlations between mode frequencies of FEM and beam,
- the thermal analogy on the FEM blade,
- and will provide CFD coupled results in hover and forward flight.

7 Acknowledgments

The financial support received by the Defence, Science and Technology Laboratory (DSTL) of UK, under contract No. DSTLX10000129255 is gratefully acknowledged.

Part of the results were obtained using the ARCHIE-WeSt High Performance Computer (www.archie-west.ac.uk). EPSRC grant no. EP/K000586/1 and Cirrus UK National Tier-2 HPC Service at EPCC (http://www.cirrus.ac.uk).

This work is part of the Smart Twisting Active Rotor (STAR) project. The authors would like to thank the STAR project partners for the useful discussions in active twist blade modelling. The additional information provided by DLR to develop the approximate finite element models used in this work is gratefully acknowledged.

References

[1] Shin, S., Cesnik, C., and Hall, S., "Closed-loop control test of the NASA/Army/MIT Active Twist Rotor for vibration reduction," *Journal of the American Helicopter Society*, Vol. 50, No. 2, 2005, pp. 178–194.

[2] Wierach, P., Riemenschneider, J., Optiz, S., and Hoffmann, F., "Experimental investigation of an active twist model rotor blade under centrifugal loads," *33rd European Rotorcraft Forum, ERF33*, Vol. 3, Kazan, Russia, September 2007, pp. 1653–1665.

[3] van der Wall, B. G., Lim, J. W., Riemenschneider, J., Kalow, S., Wilke, G. A., D. Douglas, J. B., Bailly, J., Delrieux, Y., Cafarelli, I., Tanabe, Y., Sugawara, H., Jung, S. N., Hong, S. H., Kim, D.-H., Kang, H. J., Barakos, G., and Steininger, R., "Smart twisting active rotor (STAR) - Pre-test predictions," *48th European Rotorcraft Forum*, Winterthur, Switzerland, September 2022.

[4] Derham, R., Weems, D. B., Mathew, M. B., and Bussom, R. C., "The design evolution of an active materials rotor," *The American Helicopter Society Forum 57*, Washington, D.C., USA, 2001.

[5] Weems, D. B., Anderson, D., Mathew, M. B., and Bussom, R. C., "A large-scale active twist rotor," *The American Helicopter Society Forum 60*, Baltimore, MD, USA, June 2004.

[6] Haehnel, R., Lim, J., Wenren, Y., Tain, S., and Yu, W., "Structural Analysis of a Rotorcraft Blade Design Using iVABS," *Vertical Flight Society, Forum 79*, West Palm Beach, FL, USA, 2023.

[7] Ahn, J. H., Hwang, H. J., Chang, S., Jung, S. N., Kalow, S., and Keimer, R., "X-ray Computed Tomography Method for Macroscopic Structural Property Evaluation of Active Twist Composite Blades," *Aerospace*, Vol. 8, No. 12, 2021.

[8] Wilkie, W. K., Bryant, R. G., High, J. W., Fox, R. L., Hellbaum, R. F., Jalink, A. J., Little, B. D., and Mirick, P. H., "Low-cost piezocomposite actuator for structural control applications," *Smart Structures and Materials 2000: Industrial and Commercial Applications of Smart Structures Technologies*, edited by J. H. Jacobs, Vol. 3991, International Society for Optics and Photonics, SPIE, 2000, pp. 323 – 334.

[9] Steijl, R., Barakos, G. N., and Badcock, K., "A framework for CFD analysis of helicopter rotors in hover and forward flight," *International Journal for Numerical Methods in Fluids*, Vol. 51, No. 8, 2006, pp. 819–847.

[10] Osher, S. and Chakravarthy, S., "Upwind schemes and boundary conditions with applications to Euler equations in general geometries," *Journal of Computational Physics*, Vol. 50, No. 3, 1983, pp. 447–481, DOI: 10.1016/0021-9991(83)90106-7.

[11] van Leer, B., "Towards the ultimate conservative difference scheme. V.A second-order sequel to Godunov's Method," *Journal of Computational Physics*, Vol. 32, No. 1, 1979, pp. 101–136, DOI: 10.1016/0021-9991(79)90145-1.

[12] van Albada, G. D., van Leer, B., and Roberts, W. W., "A Comparative Study of Computational Methods in Cosmic Gas Dynamics," *Astronomy and Astrophysics*, Vol. 108, No. 1, 1982, pp. 76–84, DOI: 10.1007/978-3-642-60543-7.

[13] Jameson, A., "Time-Dependent Calculations Using Multigrid, with Applications to Unsteady Flows past Airfoils and Wings," *AIAA 10th Computational Fluid Dynamics Conference*, 1991.

[14] Axelsson, O., *Iterative Solution Methods*, Cambridge University Press: Cambridge, MA, 1994, DOI: 10.1017/CBO9780511624100.

[15] Menter, F. R., “Two-Equation Eddy-Viscosity Turbulence Models for Engineering Applications,” *AIAA Journal*, Vol. 32, No. 8, 1994, pp. 1598–1605.